The Astrophysical Journal, 843:79 (9pp), 2017 July 10 https://doi.org/10.3847/1538-4357/aa775e

Star Formation at $z = 2.481$ in the Lensed Galaxy SDSS J1110+6459. II. What is Missed at the Normal Resolution of the *Hubble Space Telescope*?

J. R. Rigby[1], T. L. Johnson[2], K. Sharon[2], K. Whitaker[3,4,10], M. D. Gladders[5,6], M. Florian[5], J. Lotz[7], M. Bayliss[8], and E. Wuyts[9]
[1] Observational Cosmology Lab, NASA Goddard Space Flight Center, 8800 Greenbelt Rd., Greenbelt, MD 20771, USA
[2] Department of Astronomy, University of Michigan, 500 Church St., Ann Arbor, MI 48109, USA
[3] Department of Astronomy, University of Massachusetts, 710 N Pleasant St., Amherst, MA 01003, USA
[4] Department of Physics, University of Connecticut, 2152 Hillside Rd. Unit 3046, Storrs, CT 06269, USA
[5] Department of Astronomy & Astrophysics, University of Chicago, 5640 S. Ellis Ave., Chicago, IL 60637, USA
[6] Kavli Institute for Cosmological Physics, University of Chicago, 5640 South Ellis Ave., Chicago, IL 60637, USA
[7] Space Telescope Science Institute, 3700 San Martin Dr., Baltimore, MD 21218, USA
[8] Department of Physics, Massachusetts Institute of Technology, Cambridge, MA, 02139
[9] ArmenTeKort, Antwerp, Belgium
Received 2017 March 9; revised 2017 May 22; accepted 2017 June 1; published 2017 July 6

Abstract

For lensed galaxy SGAS J111020.0+645950.8 at redshift $z = 2.481$, which is magnified by a factor of 28 ± 8, we analyze the morphology of star formation, as traced by rest-frame ultraviolet emission, in both the highly magnified source plane and simulations of how this galaxy would appear without lensing magnification. Were this galaxy not lensed, but rather drawn from a *Hubble Space Telescope* deep field, we would conclude that almost all its star formation arises from an exponential disk (Sérsic index of 1.0 ± 0.4) with an effective radius of $r_e = 2.7 \pm 0.3$ kpc measured from two-dimensional fitting to F606W using Galfit, and $r_e = 1.9 \pm 0.1$ kpc measured by fitting a radial profile to F606W elliptical isophotes. At the normal spatial resolution of the deep fields, there is no sign of clumpy star formation within SGAS J111020.0+645950.8. However, the enhanced spatial resolution enabled by gravitational lensing tells a very different story; much of the star formation arises in two dozen clumps with sizes of $r = 30$–50 pc spread across the 7 kpc length of the galaxy. The color and spatial distribution of the diffuse component suggests that still-smaller clumps are unresolved. Despite this clumpy, messy morphology, the radial profile is still well-characterized by an exponential profile. In this lensed galaxy, stars are forming in complexes with sizes well below 100 pc; such sizes are wholly unexplored by surveys of galaxy evolution at $1 < z < 3$.

Key words: galaxies: star formation – gravitational lensing: strong – ultraviolet: galaxies

1. Introduction

The diffraction limit of the *Hubble Space Telescope* (*HST*), $\lambda/D = 0\farcs033$ and $0\farcs052$ at wavelengths of 3900 Å and 6060 Å, corresponds to physical scales of 270 and 420 pc at $z = 2.5$. By contrast, the typical sizes of the H II regions that host new stars are typically less than $D \sim 100$ pc (c.f. Liu et al. 2013). As such, diffraction limits our ability to spatially resolve where stars form in galaxies in the distant universe.

Recent work has focused on bright clumps of star formation in distant galaxies (e.g., Elmegreen & Elmegreen 2005; Elmegreen et al. 2007, 2009), with typical sizes of ~1 kpc (Förster Schreiber et al. 2011). These clumps may arise from gravitational instabilities in gas-rich disks (Toomre 1964; Genzel et al. 2011), or where cold gas has accreted onto the disk (Kereš et al. 2005; Dekel & Birnboim 2006; Brooks et al. 2009). However, the physical scales of these clumps are close to the diffraction limit of *HST*; it is plausible, even likely, that many of these clumps are collections of smaller structures that are blurred together at the spatial resolution of *HST* (Fisher et al. 2016; Tamburello et al. 2017). We have very little evidence as to the presence or importance of star formation on small ($\lesssim$100 pc) scales in distant galaxies. Indeed, this absence of evidence motivates future missions: the science goals for a conceptual ~10 m ultraviolet and optical space telescope include mapping and spectroscopically dissecting star-forming regions in distant galaxies down to 100 pc scales (Dalcanton et al. 2015).

Gravitational lensing provides rare opportunities to overcome the *HST* diffraction limit and study star formation in distant galaxies on small spatial scales (e.g., Swinbank et al. 2009; Livermore et al. 2012). Johnson et al. (2017b, hereafter Paper I) present a detailed lensing model for galaxy cluster SDSS J1110+6459, using a hybrid parametric/non-parametric strong lensing mass model. They use a novel forward-modeling technique to reconstruct in the source plane the bright lensed galaxy that it is magnifying, SGAS J111020.0+645950.8 (hereafter SGAS 1110). Simulations showed the clump-finding algorithm was 80% complete down to an intrinsic clump brightness of $m_{AB}(F606W) = 33.2$, and that the resolution limit is roughly 20 pc. Paper I identified two dozen ultraviolet-bright clumps in this highly magnified lensed galaxy. Johnson et al. (2017a, hereafter Paper III) find that the clump size distribution function is dominated by small clumps with inferred radii of $r = 30$–50 pc. As such, SGAS 1110 provides the best opportunity yet to study, at a high spatial resolution not normally achievable, the morphology of star formation in a galaxy at redshift $z = 2.5$.

In this paper, we simulate what SGAS 1110 would look like to *HST* were it not lensed, but merely a field galaxy in a deep survey such as CANDELS (Grogin et al. 2011). We analyze its size, structure, and morphology at this native unlensed (or "candelized" resolution) and compare it to the morphology inferred from the reconstructed lensed images. Using the test case of SGAS 1110, we explore how inferences about star

[10] Hubble Fellow.

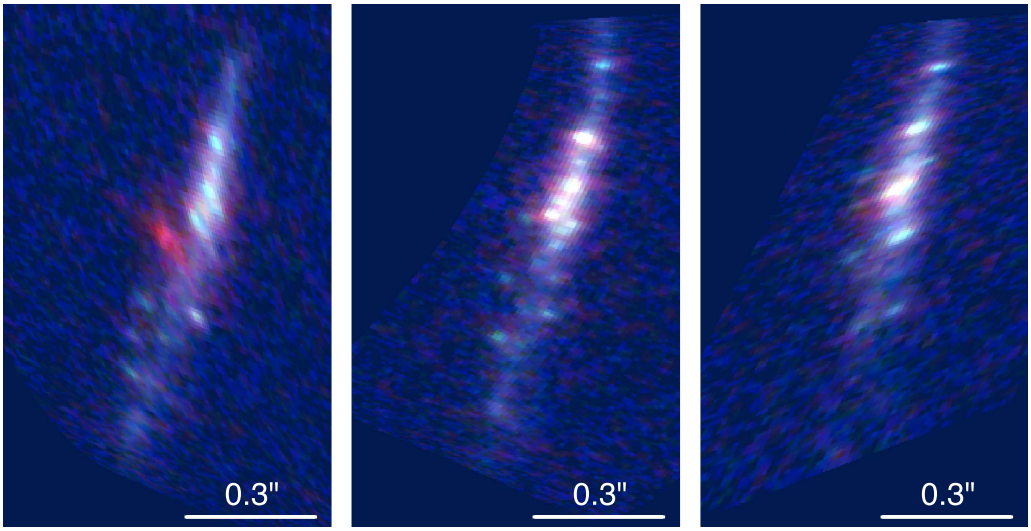

Figure 1. Source-plane reconstructions of lensed galaxy SGAS J111020.0+645950.8 at $z = 2.481$. Shown are reconstructions from three images of the lensed galaxy: A1 (left panel), A2 (middle panel), and A3 (right panel). Image A2 is the most highly magnified, and therefore reveals the most detail. Image A1 suffers from a contaminating cluster galaxy. The BGR composite is comprised of F390W, F606W, F105W; the stretch is linear. A scalebar of $0\farcs3$ is shown.

formation in the distant universe depend on the available spatial resolution. Finally, we simulate what SGAS 1110 would look like, were it not lensed, to *JWST* and a future large optical space telescope.

We assume a flat cosmology with $\Omega_M = 0.3$, $\Omega_\Lambda = 0.7$, and $H_0 = 70$ km s^{-1} Mpc^{-1}. In this cosmology, an angular size of $1''$ corresponds to an angular diameter distance of 8.085 kpc at the redshift of SGAS 1110 at $z = 2.481$.

2. Methods

2.1. Imaging Data

The data used in this paper are *HST* WFC3 images in the F390W, F606W, F105W, and F160W filters from *HST* program GO 13003 (PI Gladders), and derivative source-plane reconstructions, as described in Paper I and shown in Figure 1. The data are comparatively shallow: a single orbit in each optical band, and half orbit in each infrared band, taken as part of a survey with many targets.

The 5σ limiting magnitudes (not corrected for lensing) quoted in Paper I in F390W, F606W, F105W, and F160W are 2.5,[11] 5.7, 3.8, and 4.8 mag shallower than the limits quoted for the CANDELS deep program, and[12] 5.1, 3.1, and 4.1 mag shallower than the CANDELS wide program.[13] The total magnification of the giant arc SGAS 1110 is 28 ± 8. Thus, on average, the intrinsic depth of the *HST* data for image A2 of SGAS 1110 is comparable to the depth of the CANDELS deep surveys in F105W, 1 mag deeper in the blue (F390W), and 1.4–2 mag shallower in F606W.

Lensing magnification has made the SGAS 1110 data roughly comparable in effective depth to CANDELS; we have not attempted to match depths exactly—for example, by adding additional noise. Instead, as described in the next subsection, we have matched the spatial resolution of such observations.

[11] CANDELS did not use the F390W filter; accordingly, for CANDELS Deep, we quote the depth in the F336W filter.
[12] CANDELS Wide did not use the F390W or a similar filter.
[13] Using 5σ magnitude limits from http://candels.ucolick.org/survey/Survey_Desc.html.

2.2. Reconstructed Images

We reconstruct all three images of the galaxy SGAS 1110 in the source plane using the methods described in Sharon et al. (2012, 2014) and Sharon & Johnson (2015), by ray-tracing each pixel from the image plane to the source plane. These are the reconstructions used for most of this paper. The exception is when we simulate images from a future large ultraviolet and optical telescope (Section 2.4 and Figure 4), where the highest possible spatial resolution is needed. For those simulations, we use as input the best-fit model of clump positions, sizes, and brightnesses, and the best-fit model of the smooth component, for F390W and F606W, all in the source plane, from Paper I. That model resulted from a forward modeling technique to model the sizes and brightnesses of clumps in the source plane, which effectively deconvolves the source galaxy from the effects of the lensing point-spread function (PSF).

2.3. Convolving to the Unlensed Resolution of HST

We degraded the source-plane reconstructions to the unlensed resolution of *HST* as follows. This procedure was done for each of the three images of the arc: A1, A2, and A3.

For each filter, we used an empirical PSF determined from images of 37 lensing clusters observed in *HST* program GO 13003. The PSFs were created from stars selected based on the ratio of flux within a $2''$ aperture relative to a $0\farcs5$ aperture. The selected stars were background subtracted and centered, $>3\sigma$ background features and nearby objects were masked out, and the stars were then averaged to generate a high signal-to-noise ratio empirical PSF for each filter.

For each filter, the empirical PSF was resampled to the same pixel scale as the source-plane reconstruction, $0\farcs003$ pix^{-1}; and then convolved with the source-plane reconstruction for that filter, using the convolve_fft function within the astropy.convolution Python package.

A cluster galaxy contaminates the source-plane reconstruction of image A1. Using Galfit (Peng et al. 2010), we removed this cluster galaxy from the F160W and F105W image-plane images. Subtraction residuals can be seen in Figure 2.

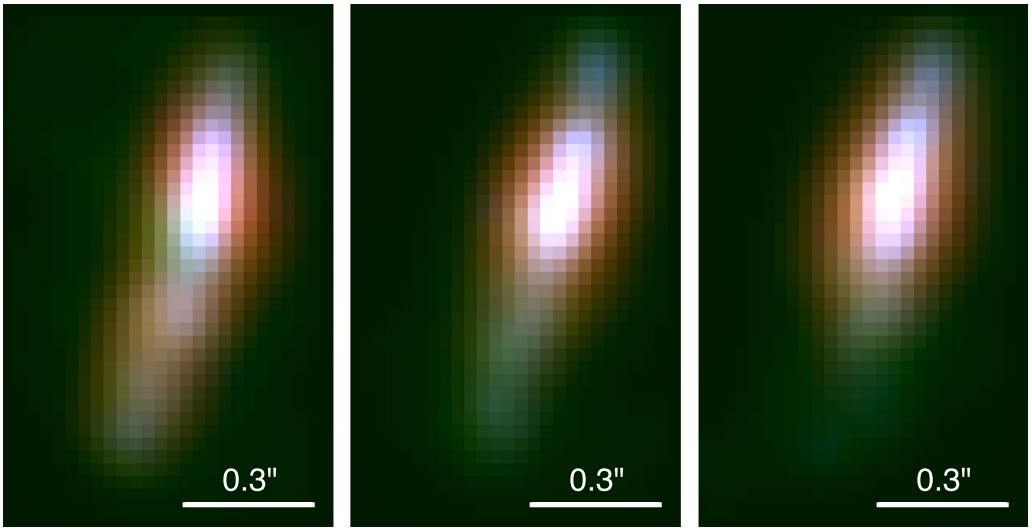

Figure 2. Simulations of how SGAS 1110 would appear to *HST* were it not gravitationally lensed, but rather a field galaxy. Shown are the simulated deep-field images generated from three separate images of the lensed galaxy: A1, A2, and A3. Each filter was "candelized" by convolving the source-plane reconstruction with an empirical *HST* PSF for that filter, and rebinning to a pixel scale of $0\farcs03$. The BGR composite is the same as Figure 1. A contaminating cluster galaxy has been subtracted from the F105W of image A1 (left image); an artifact of over-subtraction is visible.

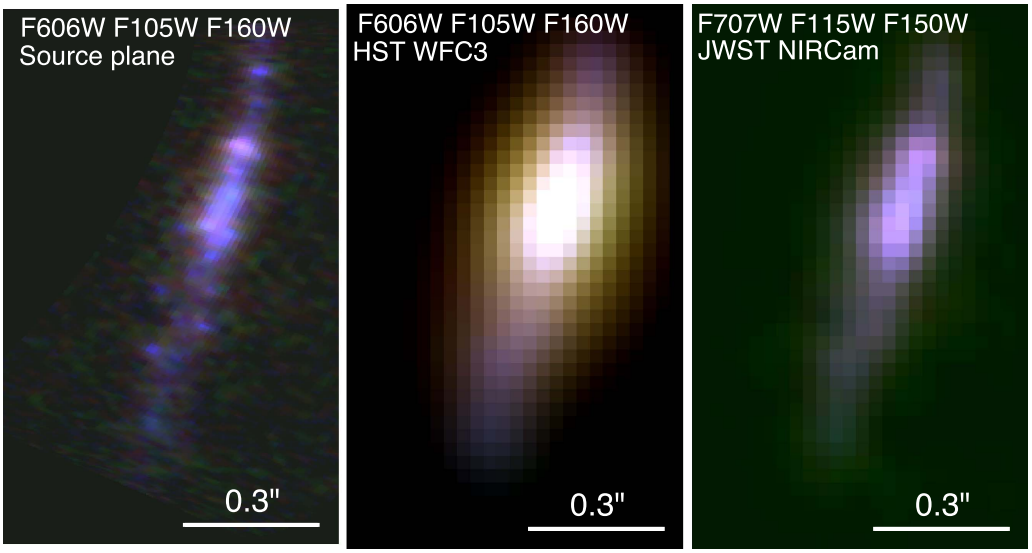

Figure 3. Simulation of how SGAS 1110 without lensing would look to WFC3/*HST* and NIRCam/*JWST*. Left panel: *HST* WFC3 source-plane image in F606W, F105W, and F160W. Middle panel: *HST* WFC3 simulated without lensing in F606W, F105W, and F160W; Right panel: *JWST* NIRCam simulated without lensing in F707W, F115W, and F150W. Lensed image A2 was the input for these simulations.

We then rebinned each convolved image to an output pixel scale of $0\farcs03\,\mathrm{pix}^{-1}$. These images have been resampled to the normal unlensed spatial resolution of *HST*, with a depth approximating deep surveys like CANDELS. These "candelized" images—or simulated deep field images—are shown in Figure 2.

2.4. Convolving to the Unlensed Resolution of JWST and LUVOIR

Similarly, we simulated the expected spatial resolution of *JWST* by convolving the source-plane images with theoretical PSFs from a library, version "revV-1,"[14] generated by Marshall Perrin's WebbPSF tool (Perrin et al. 2014). These assume the optical error budget from the *JWST* mission critical design review. The WFC3 filters F606W, F105W, and F160W were mapped to their closest NIRCam equivalents: F707W, F115W, and F150W.

We also convolved to the expected spatial resolution of a diffraction-limited, large, space-based ultraviolet/optical/infrared telescope ("LUVOIR"), using the F390W source-plane image of SGAS 1110 A2 as input (because it is the most highly magnified of the multiple images) and scaling the *HST* F390W empirical PSF by the ratio of the apertures.

These simulated images are shown in Figures 3 and 4.

2.5. Measuring Morphology

We used the morphology fitting software Galfit (Peng et al. 2010) to fit a single Sérsic component to the simulated unlensed data, separately fitting each filter and lensed image of SGAS 1110. For the PSF image required by Galfit, we used the

[14] http://www.stsci.edu/~mperrin/software/psf_library/

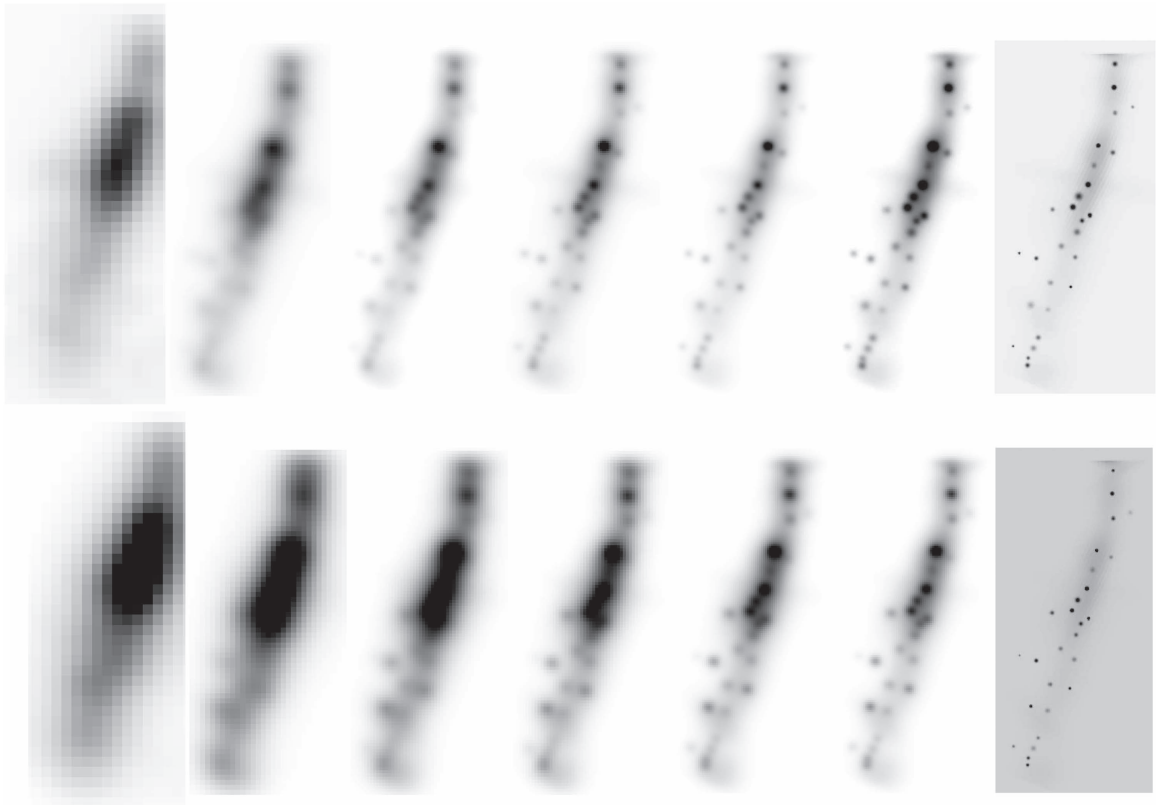

Figure 4. Simulation of how SGAS 1110 without lensing would look to a diffraction-limited large ultraviolet/optical/infrared telescope ("LUVOIR") of varying aperture size. The PSF has been scaled from the empirical *HST* PSF, and the binning is Nyquist sampled. The top panel is F390W, and the bottom panel is F606W. From left to right, the columns are: *HST* (2.4 m), 4, 6, 8, 10, 12 m, and the noise-free model of the lensed source-plane reconstruction, from which the other images were derived. Lensed image A2 was the input for these simulations. No noise has been added.

Table 1
Galfit Results, Fitting a Sérsic Component to Each Candelized Image

	Sérsic Indices					Effective Radius r_e ($''$)					Fraction of Light in Model				
Filter	A1	A2	A3	Mean	std	A1	A2	A3	Mean	std	A1	A2	A3	Mean	std
F390W	1.44	1.50	0.95	1.29	0.30	0.35	0.34	0.27	0.32	0.043	0.86	1.00	0.92	0.93	0.07
F606W	1.10	1.54	0.99	1.21	0.29	0.35	0.36	0.29	0.33	0.041	0.89	1.00	0.97	0.96	0.06
F105W	0.36	1.23	0.70	0.77	0.44	0.37	0.31	0.26	0.31	0.055	1.12	1.00	0.99	1.04	0.07
F160W	0.38	0.84	0.83	0.68	0.26	0.35	0.31	0.29	0.32	0.029	0.92	0.95	0.96	0.94	0.02

Note. Effective radii are quoted in arcseconds; the pixel scale was $0\farcs03$ per pixel.

same empirical PSF used to degrade the resolution. For the uncertainty required by Galfit, we used a constant uncertainty for each image that is the standard deviation of counts.

We fit elliptical isophotes to the source-plane images and the simulated deep-field images using the Iraf package stsdas.analysis.isophote.ellipse. We analyzed the F606W filter because inspection proves it is sensitive to fainter clumps of rest-frame ultraviolet emission than is F390W; we focused on lensed image A2 because it has the highest magnification of the lensed images of SGAS 1110. We use the technique of Szomoru et al. (2010) to account for the PSF; in short, we add the residuals from the Sérsic fitting to the best-fit Sérsic model (without the PSF), and fit ellipses to that.

The non-parametric morphology statistics—Gini coefficient, M_{20}, concentration, and asymmetry—were measured for the source-plane images and the simulated deep field images in each band, using the approach described in Lotz et al. (2004) and Peth et al. (2016). The Gini coefficient (G, Lorenz 1905; Abraham et al. 2003; Lotz et al. 2004) quantifies the inequality of the light distribution in a galaxy; it is measured using a galaxy's pixels with surface brightnesses greater than the surface brightness at its Petrosian radius (Petrosian 1976). M_{20} is the normalized second-order moment of the brightest regions of the pixels (using the pixel selection as for G), and quantifies the spatial distribution of bright knots. Concentration (C; Bershady et al. 2000; Conselice 2003) is the ratio of the circular radius containing 80% (r_{80}) of a galaxy's light (as measured within 1.5 Petrosian radii) to the radius containing 20% (r_{20}) of the light. Asymmetry (A) is the background-corrected difference between the image of a galaxy and the image rotated by 180°, measured with 1.5 Petrosian radii. G–M_{20}, and C–A have been found to separate galaxies with disturbed or multiply-nucleated morphologies from disk and bulge-dominated systems (Conselice 2003; Lotz et al. 2004, 2008; Peth et al. 2016).

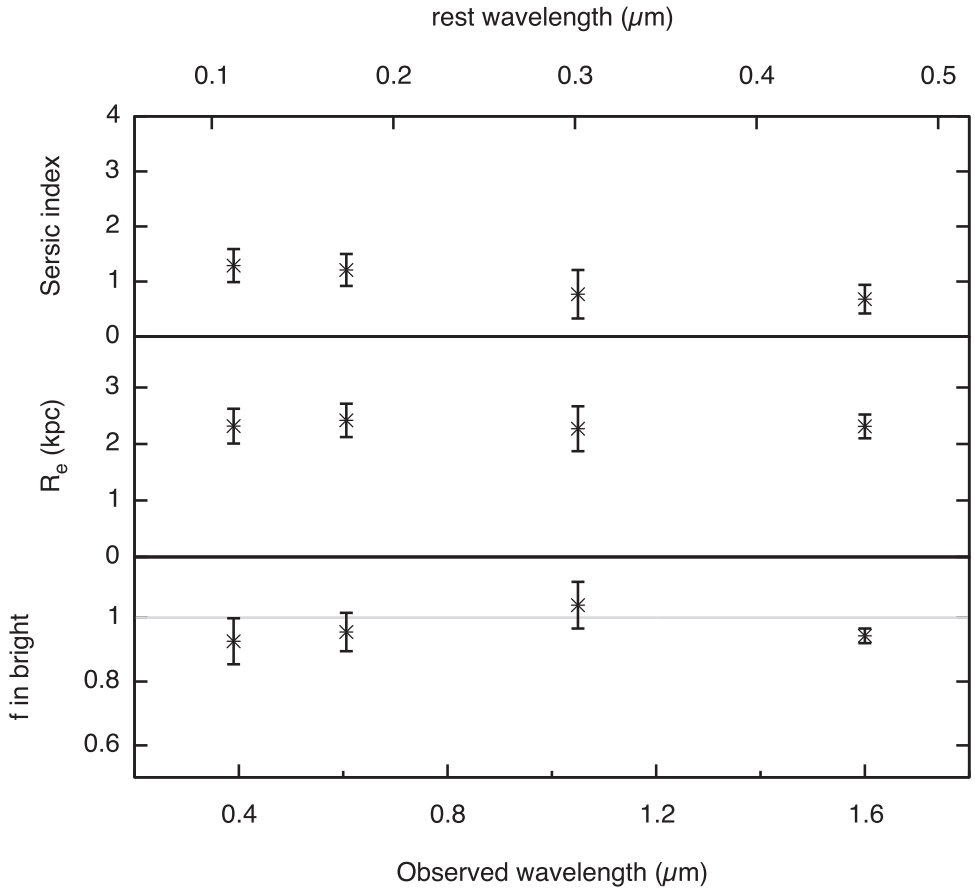

Figure 5. Results of fitting a single bright component to each simulated deep field image of SGAS 1110. Plotted are the Sérsic index, effective radius, and fraction of the total light fit by that single component. Measurements were made separately for each of the three lensed images of SGAS 1110. For each filter, we plot the average of the measurements and standard deviation. These measurements are tabulated in Table 1.

3. Results

3.1. Star Formation Rate and Stellar Mass

We measure integrated photometry of the lensed images of SGAS 1110, and fit spectral energy distribution models as in Wuyts et al. (2014), to constrain the following observed quantities (not corrected for lens magnification):

1. age of 200 Myr (range 100–380);
2. extinction of $A_v = 0.0$ (range 0.0–0.2);
3. stellar mass of $\log(M_*) = 10.68\ M_\odot$ (range 10.53–10.79);
4. star formation rate of $230\ M_\odot\ \mathrm{yr}^{-1}$ (range 220–440).

To translate into intrinsic quantities, we compute the appropriate magnification by taking the ratio of the area of the photometry aperture in the image plane to the ray-traced area of that aperture in the source plane. We compute this magnification for each of the eight lens models in Paper I; the median and median absolute deviation of the magnifications is 28 ± 8.

As such, we estimate the intrinsic quantities as:

1. Stellar mass of $\log M^* = 9.24\ M_\odot$, with associated uncertainties of $^{+0.11}_{-0.15}$ from SED fitting and $^{+0.08}_{-0.12}$ from the magnification uncertainty.
2. Star formation rate as $8.5\ M_\odot\ \mathrm{yr}^{-1}$, with associated uncertainties of $^{+8}_{-0.4}$ from SED fitting and $^{+4}_{-2}$ from the magnification uncertainty.

3.2. Clumpiness and Color

The discrete rest-frame ultraviolet clumps identified in Paper I contain a total of 23% (22%) of the light in the F390W (F606W) filter in the image plane. Formally, these measurements are lower limits on the percent of the light in clumps; there are doubtless clumps too faint or too small for our data to identify, which we have lumped into the "smooth" component.

We measure the rest-frame ultraviolet color of the clumps and the diffuse emission, at the full spatial resolution offered by gravitational lensing. The mean color and standard deviation of the clumps is $F390W - F606W = 0.48 \pm 0.39$, as measured in the source plane. For the smooth component, we measure the flux-weighted color in the image plane to be $F390W - F606W = 0.45 \pm 0.05$, with negligible variation in color depending on the surface brightness cut adopted. Thus, the clumpy and diffuse emission have the same average color within uncertainties, implying similar stellar populations and reddening. The spatial distribution of the smooth component also closely traces the spatial distribution of the clumps; see Figure 9 of Paper I.

3.3. Size and Structure

At the full spatial resolution, the majority of the rest-frame ultraviolet light (52% percent, measured in either F390W or

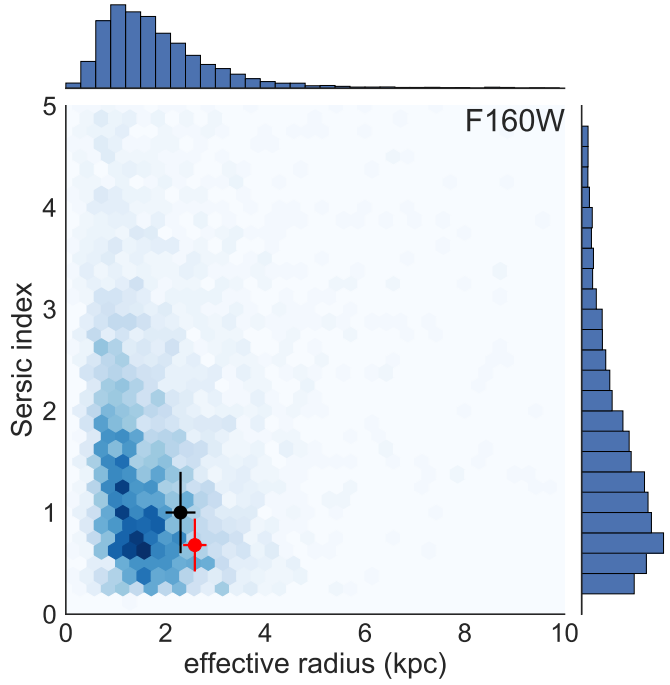

Figure 6. Comparison of Sérsic indices and effective radii to CANDELS. A density map shows measurements for the galaxies in the catalogs of van der Wel et al. (2012) that have good Galfit fits ("FLAG = 0") in the F160W filter, 3D-*HST* "best" redshift of $2 < z < 3$, and stellar masses of $9.0 < \log M^* < 9.5\ M_\odot$ from 3D-*HST* (Momcheva et al. 2015). The red point shows our measurement for the simulated deep field F160W image of SGAS 1110, using Galfit, from Section 3.3. The black point shows the average measurements for the simulated deep-field images in all four bands. Histograms of effective radius and Sérsic index are shown in the margins. In F160W, the CANDELS subset has $R_e = 1.7 \pm 0.7$ kpc (median ± median absolute deviation), compared to $R_e = 2.6 \pm 0.2$ kpc for SGAS 1110 in that filter.

F606W) in SGAS 1110 is concentrated within the central 0.″3 (2.4 kpc).

At the normal resolution of *HST* deep fields, an extended central component contains most of the flux. The single Sérsic component fit by Galfit that best fits each image (averaging over all four bands and all three images) has a Sérsic index of 1.0 ± 0.4 and an effective radius of 2.3 ± 0.3 kpc; that component contains 97% ± 7% of the total light. Table 1 lists these results for each filter and each image of the lensed arc. Figure 5 shows moderate trends with wavelength, which are unsurprising given the factor of three difference in diffraction–limited resolution between the bluest (F390W) and the reddest (F160W) filters.

We now contextualize the physical sizes we measure with Galfit for the simulated deep field images of SGAS 1110, with measurements and samples from the literature. We first consider the older stellar population, using the F160W filter. Van der Wel et al. (2012) fit Galfit profiles to a large sample of unlensed galaxies from the CANDELS survey. From the catalogs of van der Wel et al. (2012) and Momcheva et al. (2015), we select a subset of galaxies at redshift and stellar mass matched to SGAS 1110. These have an acceptable Galfit fit (flag = 0) in the F160W filter, a 3D-*HST* "best redshift" of $2 < z < 3$, and a stellar mass in the range $9.0 < \log M^* < 9.5\ M_\odot$. A total of 160W galaxies satisfy these criteria. Figure 6 compares the results for this matched sample to those of SGAS 1110. The Sérsic indices we measure for the simulated deep field SGAS 1110 images are entirely consistent with the average Sérsic index from van der Wel et al. (2012). This CANDELS subset has $R_e = 1.6 \pm 0.6$ kpc (median ± median absolute deviation) for F160W, compared to $R_e = 2.6 \pm 0.2$ kpc for SGAS 1110 in F160W. Thus, in F160W, SGAS 1110 has an effective radius that is larger than average, but well within the observed range, of galaxies at matched stellar mass and redshift.

We examine this result's sensitivity to age by dividing the 3D-*HST* galaxies into two groups with specific star formation rates (as listed in the 3D-*HST* catalog) above or below 1 Gyr^{-1}. The older and younger subsets have, respectively, effective radii in F160W of $R_e = 1.55 \pm 0.64$ kpc and $R_e = 1.70 \pm 0.64$ kpc (median and median absolute deviation). Thus, the galaxies with younger ages have somewhat larger sizes.

We repeat this analysis for the filter F125W. In F125W, a total of 125W galaxies in van der Wel et al. (2012) satisfy the redshift and stellar mass ranges. These have a median effective radius of $R_e = 1.7 \pm 0.7$ kpc (median ± median absolute deviation). The older and younger subsamples, respectively, have $R_e = 1.66 \pm 0.68$ kpc and $R_e = 1.74 \pm 0.65$ kpc. These results are consistent with those for F160W.

Figure 7 plots the radial profiles of F606W surface brightness that resulted from fitting elliptical isophotes to lensed image A2. The isophotes of both the source-plane image and the simulated deep field image are fit well by exponential profiles. For an exponential profile, the disk scale length r_s is related to the effective radius r_e as: $r_e = 1.678\ r_s$. Converting the effective radii from the elliptical isophote fitting yields $r_e = 1.5 \pm 0.1$ kpc for the source-plane image and $r_e = 1.9 \pm 0.1$ kpc for the simulated deep field image, both in F606W.

These sizes are somewhat smaller than the typical effective radii of $r_e = 2.5$ kpc measured by (Elmegreen et al. 2005) for disk galaxies in the *HST* ultra-deep field, as measured with the ACS F775W filter.

Comparing these multiple measurements, for the elliptical isophote fitting larger sizes are measured from the simulated deep fields than from the source-plane reconstructions; this is presumably a resolution effect. For the simulated deep fields, the two-dimensional Galfit fitting returns a size that is 1.3σ larger than derived from elliptical isophote fitting.

3.4. Quantitative Morphology

In Figure 8, we compare the quantitative morphological measurements of Gini, M20, concentration, and asymmetry of SGAS 1110 to those measured for CANDELS galaxies matched in redshift and stellar mass ($2 < z < 3, 9.0 < \log(M_*/M_\odot < 9.5$). We consider the filters F606W, F105W, and F160W, and measure at both the source-plane resolution and at the simulated deep-field resolution. We find negligible difference between C, G, and M_{20} values for the source-plane and simulated deep-field versions of the SGAS 1110 measures. The measured asymmetry values for the source-plane images are unphysically negative, likely due to an overcorrection for the asymmetry of the background.

SGAS 1110 would likely be classified as a "Group 1 galaxy" (Peth et al. 2016), meaning it has a late-type disk without a prominent bulge. Its asymmetry is insufficiently high to be considered a merger; neither G nor M_{20} is high, indicating that SGAS 1110 does not have any particularly prominent clumps. Compared to the morphology distributions of matched CANDELS galaxy sample, SGAS is a typical disk galaxy for its redshift and stellar mass.

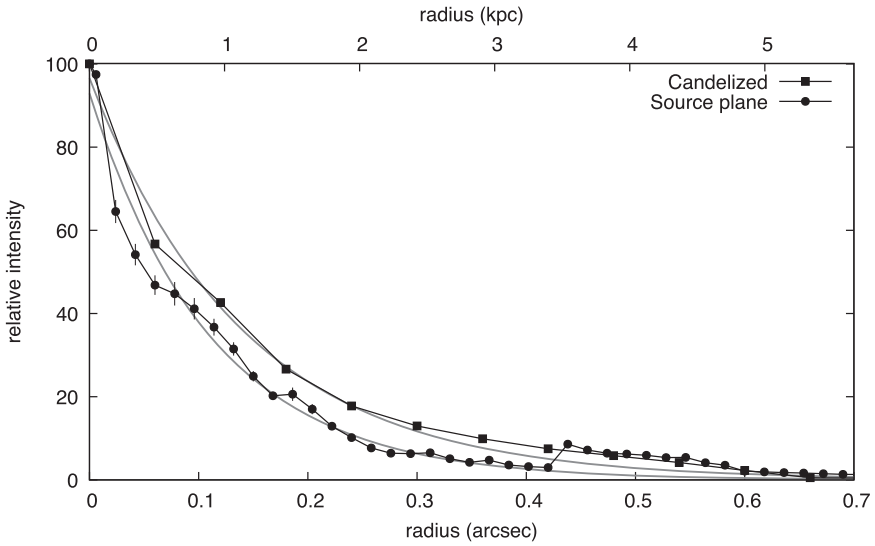

Figure 7. Distribution of intensity with radius, from isophotal ellipses fit to the source plane F606W reconstruction of A2 (filled circles) and the simulated deep field F606W for A2 (filled squares), using the method of Szomoru et al. (2010) to account for the PSF. The best-fitting exponential profiles are overplotted in gray. The profiles have been scaled to a relative intensity of 100 at $R = 0$.

4. Discussion

SGAS 1110 is a rare case where high lensing magnification provides a much sharper view of a distant galaxy than is normally possible. It is therefore appropriate to take the lensing reconstruction as the "true image" and consider to what extent deep, non-lensed *HST* images could recover that morphology.

In short, at the normal spatial resolution of *HST*, SGAS 1110 is correctly classified as a non-merging disk galaxy; its size is correctly measured, as is the fact that its light profile is exponential. What is missed, however, is extreme clumpiness of the star formation on $<$100 pc scales.

Were SGAS 1110 not gravitationally lensed, but instead drawn from an *HST* deep field, we would conclude that almost all of the star formation emerges from an exponential disk (Sérsic index of 1.2 ± 0.3 in F606W) with an effective radius of $r_e = 2.7 \pm 0.3$ kpc measured from two-dimensional fitting to F606W using Galfit, and $r_e = 1.9 \pm 0.1$ kpc measured from 1D fits to the elliptical isophotes, after correcting for the PSF. For its stellar mass and redshift, SGAS 1110 at F160W ($\lambda_{\rm rest} \sim 0.65$ μm) appears larger than average, but well within the observed range. In the rest-frame ultraviolet as probed by the F390W and F606W filters ($\lambda_{\rm rest} \sim 0.1$–$0.3$ μm), we were unable to find a matched sample, but the size of SGAS 1110 appears typical of those measured for star-forming galaxies at lower or similar redshift.

Quantitative morphological measures would classify SGAS 1110 as a disk galaxy, without signs of a merger or prominent clumps. The non-parametric measures G, M_{20}, and C are consistent with CANDELS galaxies at this epoch and mass scale. The rest-frame $\sim$4600 Å morphology values (as probed by F160W) are comparable to those measured for local late-type Sc/Sd/dIrr galaxies (e.g., Lotz et al. 2004.) Interestingly, the quantitative morphological measurements are consistent for the simulated deep-field and full lensed resolutions. This suggests that the robustness of these measures, which has been demonstrated for spatial resolution between $\sim$100 pc and $\sim$1 kpc in local galaxies (see Figure 6 of Lotz et al. 2004), also holds for higher-redshift galaxies.

At the simulated deep-field resolution, SGAS 1110 shows no obvious off-nuclear "blobs" or "clumps" of star formation that contain more than 8% of the total UV luminosity, which is the clump definition proposed by Guo et al. (2015).

Thus, were SGAS 1110 in an *HST* deep field, one would conclude that it is an inclined galaxy undergoing centrally concentrated star formation in a smooth, $r_e = 2$ kpc exponential disk, with no off-axis clumps of star formation. How does this picture compare to that revealed by the source plane images at full spatial resolution?

The reconstructed source-plane images, which resolve clumps with radii down to $r = 30$ pc (Paper I), show that SGAS 1110 is forming stars across its 7 kpc length. Half the rest-frame ultraviolet light (52% percent, measured in either F390W or F606W) is concentrated within the central $0\farcs3$ (2.4 kpc). A significant minority of the rest-frame ultraviolet light, 23% at F390W and 22% at F606W, resolves into more than twenty discrete clumps identified in Paper I.

The smooth component and the clumps have very similar spatial distribution, and identical rest-frame ultraviolet color within uncertainties. This implies that the smooth component and the clumps have similar star formation histories and extinction. Much of that "smooth" component may be comprised of smaller star-forming regions that are still unresolved. Some of that emission could also be truly diffuse, arising from stars that escaped from short-lived star clusters, or from genuine "field" stars that were born outside star clusters (Massey et al. 1995).

Despite the extremely clumpy morphology of the star formation, the elliptical isophotes fit to the F606W source-plane reconstruction are well-described by an exponential profile. Although the two-dimensional morphology is complex, it averages out to a smooth one-dimensional surface brightness profile. As such, our results extend, down to much smaller physical scales, a result of Elmegreen et al. (2005), that clumps in UDF spiral and irregular disk galaxies follow an exponential distribution of luminosity versus radius. Those authors suggest that these clumps tidally disperse to form a disk, whereas Genzel et al. (2008) suggest they may migrate inward to build up bulges or thick disks. This result also bears on the smooth,

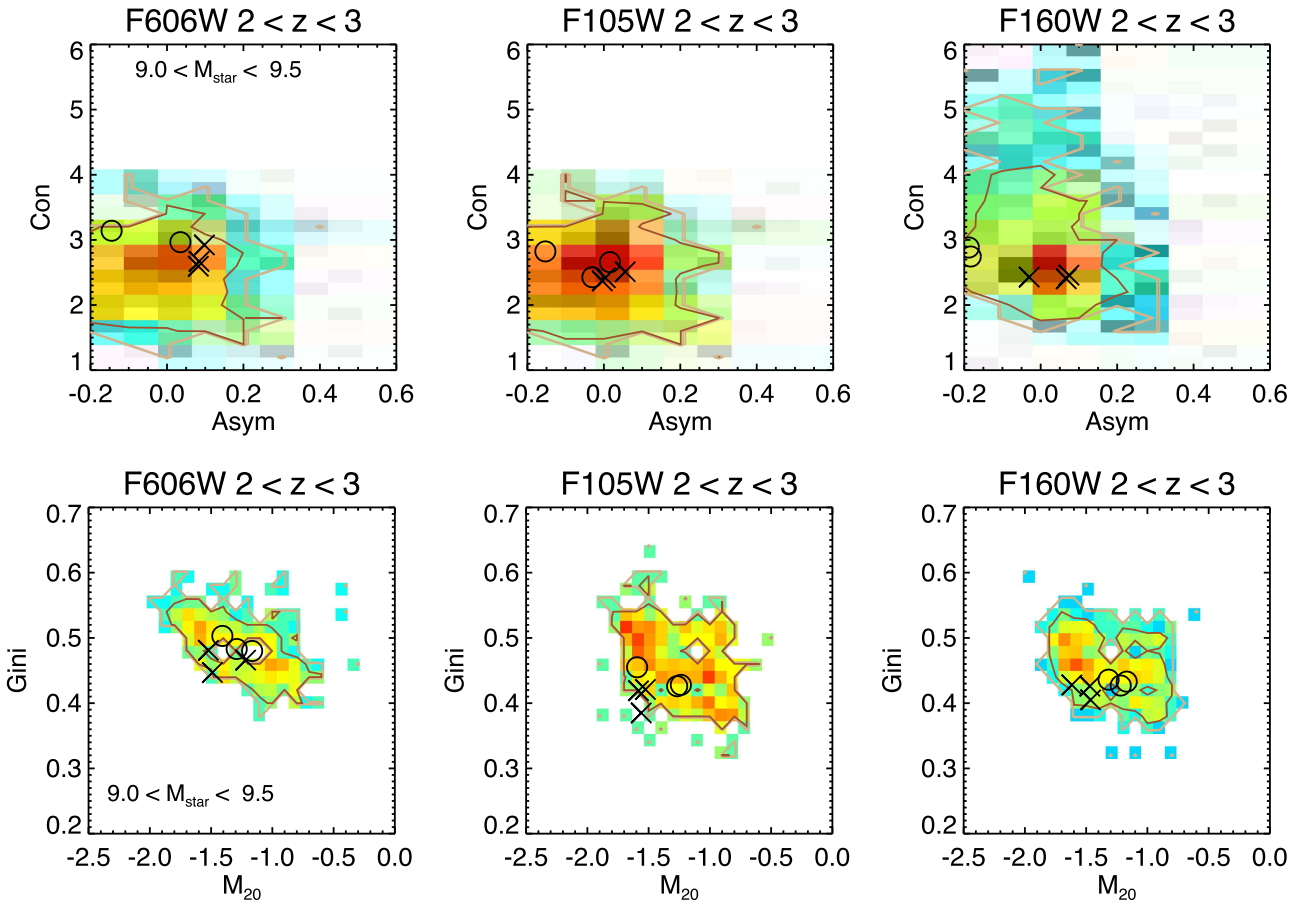

Figure 8. Quantitative morphological measurements. Measurements for SGAS 1110 are shown at the resolution of the source-plane reconstruction *(circles)*, and at the simulated deep-field resolution *(crosses)*. The background contours and color are measurements for the subset of CANDELS galaxies with redshift in the range $2 < z < 3$ and stellar mass in the range $9.0 < \log(M_*/M_\odot) < 9.5$.

large-scale formation of stars in exponential disks traced in Hα in distant galaxies by Nelson et al. (2012). Our results suggest that such star formation, which appears smooth on kiloparsec scales and when averaged over dozens of galaxies, is actually highly clumpy and messy on smaller ($\lesssim$100) parsec scales in individual galaxies.

Given the complexity of local galaxies, where stars form in star-forming regions ranging from parsec-scale single-star H II regions up to $\gtrsim$100 pc complexes like 30 Doradus and Carina, it may not be surprising that star formation in the distant universe can have significant structure on $<$100 pc scales. SGAS 1110 is the best demonstration to date that such processes are also at work in the distant universe.

Looking toward the future, our results suggest that surveys of galaxy morphology at $z \sim 1$–3 have not yet surveyed the critical size scales of star-forming regions. Figure 3 shows that *JWST* will spatially resolve some of those size scales. However, spatially resolving the dozens of star-forming regions visible in the source-plane image of SGAS 1110 would require a much larger telescope, for example, a 10 m aperture working in observed blue optical (rest-frame ultraviolet). The importance of star formation on such small physical scales at $z \sim 2$ should inform the mission concepts for future large telescopes to probe distant galaxies in the rest-frame ultraviolet. Our results imply that there is significant sub-kiloparsec structure for large future telescopes to explore with imaging and spectroscopy.

This paper is based on observations made with the NASA/ESA *Hubble Space Telescope*, obtained at the Space Telescope Science Institute, which is operated by the Association of Universities for Research in Astronomy, Inc., under NASA contract NAS 5-26555. These observations are associated with *HST* program # 13003. Support for *HST* program # 13003 was provided by NASA through a grant from the Space Telescope Science Institute, which is operated by the Association of Universities for Research in Astronomy, Inc., under NASA contract NAS 5-26555. T.L.J. acknowledges support by NASA under Grant Number NNX16AH48G. K.E.W. acknowledges support by NASA through Hubble Fellowship grant #HF2-51368 awarded by the Space Telescope Science Institute, which is operated by the Association of Universities for Research in Astronomy, Inc., for NASA, under contract NAS 5-26555. This research has made use of open-source Python packages including SciPy (http://www.scipy.org/), NumPy (Van Der Walt & Colbert 2011), IPython (Perez & Granger 2007), Pandas (McKinney 2010), and AstroPy (The Astropy Collaboration et al. 2013). J.R.R. thanks the organizers of the Python Bootcamp at the NASA Goddard Space Flight Center. J.R.R. acknowledges the hospitality of the Astronomy department at Michigan State University, where this paper was begun during a blizzard. J.R.R. is also grateful to the late Fred Lo for useful discussion and encouragement.

Facility: HST (WFC3).

References

Abraham, R. G., van den Bergh, S., & Nair, P. 2003, ApJ, 588, 218
Bershady, M. A., Jangren, A., & Conselice, C. J. 2000, AJ, 119, 2645
Brooks, A. M., Governato, F., Quinn, T., Brook, C. B., & Wadsley, J. 2009, ApJ, 694, 396
Conselice, C. J. 2003, ApJS, 147, 1
Dalcanton, J., Seager, S., Aigrain, S., et al. 2015, arXiv:1507.04779
Dekel, A., & Birnboim, Y. 2006, MNRAS, 368, 2
Elmegreen, B. G., & Elmegreen, D. M. 2005, ApJ, 627, 632
Elmegreen, B. G., Elmegreen, D. M., Fernandez, M. X., & Lemonias, J. J. 2009, ApJ, 692, 12
Elmegreen, B. G., Elmegreen, D. M., Vollbach, D. R., Foster, E. R., & Ferguson, T. E. 2005, ApJ, 634, 101
Elmegreen, D. M., Elmegreen, B. G., Ravindranath, S., & Coe, D. A. 2007, ApJ, 658, 763
Fisher, D. B., Glazebrook, K., Damjanov, I., et al. 2016, MNRAS, 464, 491
Förster Schreiber, N. M., Shapley, A. E., Genzel, R., et al. 2011, ApJ, 739, 45
Genzel, R., Burkert, A., Bouché, N., et al. 2008, ApJ, 687, 59
Genzel, R., Newman, S., Jones, T., et al. 2011, ApJ, 733, 101
Grogin, N. A., Kocevski, D. D., Faber, S. M., et al. 2011, ApJS, 197, 35
Guo, Y., Ferguson, H. C., Bell, E. F., et al. 2015, ApJ, 800, 39
Johnson, T. L., Rigby, J. R., Sharon, K., et al. 2017a, ApJL, 843, L21
Johnson, T. L., Sharon, K., Gladders, M. D., et al. 2017b, ApJ, 843, 78
Kereš, D., Katz, N., Weinberg, D. H., & Davé, R. 2005, MNRAS, 363, 2
Liu, G., Calzetti, D., Kennicutt, R. C. J., et al. 2013, ApJ, 772, 27
Livermore, R. C., Jones, T., Richard, J., et al. 2012, MNRAS, 427, 688
Lorenz, M. O. 1905, J. Am. Stat. Assoc., 9, 209
Lotz, J. M., Jonsson, P., Cox, T. J., & Primack, J. R. 2008, MNRAS, 391, 1137
Lotz, J. M., Primack, J., & Madau, P. 2004, AJ, 128, 163
Massey, P., Lang, C. C., Degioia-Eastwood, K., & Garmany, C. D. 1995, ApJ, 438, 188
McKinney, W. 2010, in Proc. of the 9th Python in Science Conf.SciPy 2010, ed. E. Jones & J. Millman, 51 (http://conference.scipy.org/proceedings/scipy2010/mckinney.html)
Momcheva, I. G., Brammer, G. B., van Dokkum, P. G., et al. 2015, arXiv:1510.02106
Nelson, E. J., van Dokkum, P. G., Brammer, G., et al. 2012, ApJL, 747, L28
Peng, C. Y., Ho, L. C., Impey, C. D., & Rix, H.-W. 2010, AJ, 139, 2097
Perez, F., & Granger, B. E. 2007, CSE, 9, 21
Perrin, M. D., Sivaramakrishnan, A., Lajoie, C.-P., et al. 2014, Proc. SPIE, 9143, 91433X
Peth, M. A., Lotz, J. M., Freeman, P. E., et al. 2016, MNRAS, 458, 963
Petrosian, V. 1976, ApJL, 209, L1
The Astropy Collaboration, Robitaille, T. P., Tollerud, E. J., et al. 2013, A&A, 558, A33
Sharon, K., Gladders, M. D., Rigby, J. R., et al. 2012, ApJ, 746, 161
Sharon, K., Gladders, M. D., Rigby, J. R., et al. 2014, ApJ, 795, 50
Sharon, K., & Johnson, T. L. 2015, ApJL, 800, L26
Swinbank, A. M., Webb, T. M., Richard, J., et al. 2009, MNRAS, 400, 1121
Szomoru, D., Franx, M., van Dokkum, P. G., et al. 2010, ApJL, 714, L244
Tamburello, V., Rahmati, A., Mayer, L., et al. 2017, MNRAS, 468, 4792
Toomre, A. 1964, ApJ, 139, 1217
Van Der Walt, S., & Colbert, S. C. 2011, CSE, 13, 22
van der Wel, A., Bell, E. F., Häußler, B., et al. 2012, ApJS, 203, 24
Wuyts, E., Rigby, J. R., Gladders, M. D., & Sharon, K. 2014, ApJ, 781, 61